Redox regulation by TXNRD3 during epididymal maturation underlies capacitation-associated mitochondrial activation and sperm motility in mice

Huafeng Wang[1], Qianhui Dou[2], Kyung Jo Jung[3], Jungmin Choi[3,4], Vadim N. Gladyshev[2], Jean-Ju Chung[1,5*]

[1]Departmet of Cellular and Molecular Physiology, Yale School of Medicine, New Haven, CT, United States

[2]Division of Genetics, Department of Medicine, Brigham and Women's Hospital, Harvard Medical School, Boston, MA, United States

[3]Department of Biomedical Sciences, Korea University College of Medicine, Seoul, South Korea

[4]Department of Genetics, Yale School of Medicine, Yale University, New Haven, CT, United States

[5]Department of Obstetrics, Gynecology, and Reproductive Sciences, Yale School of Medicine, New Haven, CT, United States

*** Correspondence:** Jean-Ju Chung (jean-ju.chung@yale.edu)

Keywords: Thioredoxin Glutathione Reductase, TXNRD3, Redox homeostasis, male fertility, mitochondrial function, Ultrastructure.

Abstract

During epididymal transit, redox remodeling protects mammalian spermatozoa, preparing them for survival in the subsequent journey to fertilization. However, molecular mechanisms of redox regulation in sperm development and maturation remain largely elusive. In this study, we report that TXNRD3, a thioredoxin reductase family member particularly abundant in elongating spermatids at the site of mitochondrial sheath formation, regulates redox homeostasis to support male reproduction. Using *Txnrd3*$^{-/-}$ mice, our biochemical, ultrastructural, and live cell imaging analyses revealed impairments in sperm morphology and motility under conditions of TXNRD3 deficiency. We reveal that mitochondria develop more defined cristae during capacitation in wild type sperm. Absence of TXNRD3 alters redox status in both the head and tail during sperm maturation and capacitation, resulting in defective mitochondrial ultrastructure and activity under capacitating conditions. These findings provide insights into molecular mechanisms of redox homeostasis and bioenergetics during sperm maturation, capacitation, and fertilization.

Introduction

Testicular sperm are functionally immature in that they lack the ability to naturally fertilize an egg. Epididymis transit is an indispensable step for mammalian sperm cells to fully develop the fertilizing ability. During epididymal descent, spermatozoa acquire the potential to develop progressive motility and capacitation (Sullivan and Mieusset 2016, Gervasi and Visconti 2017). One major threat to sperm for the subsequent journey to fertilization is oxidative damage since sperm plasma membrane is rich in polyunsaturated fatty acids (Vernet et al. 2004). Redox mechanisms prepare epididymal spermatozoa for their protection and survival during the fertilization journey (Chabory et al. 2009). For example, oxidation of the intracellular milieu is involved in mammalian sperm maturation, capacitation, acrosome reaction (de Lamirande et al. 1997, O'Flaherty 2015). At the same time, oxidative damage correlates with lower motility of human sperm (Kao et al. 2008) and causes DNA fragmentation and protein crosslinking (Henkel et al. 2005). However, it remains unclear how redox homeostasis is maintained during mammalian sperm capacitation.

Thioredoxin and glutathione systems are two major redox systems that utilize the thiol redox biology to maintain cellular redox homeostasis and protect against oxidative stress. Thioredoxin reductases, a family of selenium-containing pyridine nucleotide-disulfide oxidoreductases, are key redox regulators of mammalian thioredoxin system. They are comprised of three enzymes: thioredoxin reductase 1 (TXNRD1), thioredoxin reductase 2 (TXNRD 2) (Holmgren 1980, Mustacich and Powis 2000) and thioredoxin-glutathione reductase (TXNRD3, also known as TGR) (Sun et al. 1999, Sun et al. 2001). TXNRD1 and TXNRD2 are essential proteins that support redox homeostasis in the cytosol and mitochondria, respectively (Arnér and Holmgren 2000, Conrad et al. 2004, Nalvarte et al. 2004, Jakupoglu et al. 2005). TXNRD3 is predominantly expressed in testis (Sun et al. 2001) and particularly abundant in elongating spermatids at the site of mitochondrial sheath formation (Su et al. 2005). Structurally, TXNRD3 contains an additional N-terminal glutaredoxin domain compared with the other two TXNRD isozymes (Sun et al. 2001). Disulfide bond isomerase activity of TXNRD3 was previously reported *in vitro* (Su et al. 2005), yet the physiological significance and underlying mechanisms of TXNRD3 in male germ cell development and sperm function have been largely unknown. In the accompanying study, we

report that *Txnrd3*$^{-/-}$ mice exhibit compromised male fertility, with mild impregnation delay *in vivo* and diminished sperm fertilization capacity *in vitro* (Dou et al., 2021).

Here, we report the underlying mechanism of TXNRD3 function in regulation of chromatin organization and mitochondrial activity during sperm capacitation in mice. We find that targeted disruption of *Txnrd3* induces capacitation-associated impairment in sperm morphology and motility. Biochemical analyses demonstrate that TXNRD3 expression diminishes during sperm maturation, impairing redox homeostasis of head and flagellar proteins. Using ultrastructural analyses and live cell imaging, we reveal that mitochondria in *Txnrd3*$^{-/-}$ sperm undergo structural defects and lose control of its activity especially during sperm capacitation. These findings provide insights into sperm redox regulation during epididymal maturation and its effect on capacitation-associated energy metabolism.

Materials and methods

Mouse Sperm Preparation and *in vitro* Capacitation

Epididymal spermatozoa from adult male mice were collected by swim-out from caudal epididymis in standard HEPES saline (HS) medium (in mM, 135 NaCl, 5 KCl, 1 $MgSO_4$, 2 $CaCl_2$, 20 HEPES, 5 Glucose, 10 Lactic acid, 1 Na pyruvate, pH 7.4 adjusted with NaOH, 320 mOsm/L). 2×10^6 cells/ml sperm were incubated in human tubular fluid (HTF) medium (EMD Millipore) at 37°C, 5% CO_2 for 90 min to induce capacitation.

Antibodies and Reagents

Rabbit polyclonal antibodies specific to mouse TXNRD3 and GPX4 (Su et al. 2005) were described previously. All the other antibodies used in this study are commercially available as follows (ANT4, Abcam; P2X2, Santa Cruz; TOM20, Santa Cruz; TXNRD1, Bioss Antibodies; TXNRD2, Proteintech; acetylated tubulin, Sigma). All the chemicals were from Sigma Aldrich unless otherwise indicated.

Single-Cell RNA-Seq Analysis

The raw count matrices for human (GSE109037) and mouse (GSE109033) testis single cell RNA (scRNA)-seq datasets (Hermann et al. 2018) were downloaded from Gene Expression Omnibus (GEO) database (https://www.ncbi.nlm.nih.gov/geo/). The downloaded raw count matrices were processed for quality control using the Seurat package (ver.3.2.3) (Stuart et al. 2019). Briefly, cells with less than 200 expressed features, higher than 9,000 (GSE109033) or 10,000 (GSE109037) expressed features and higher than 20% (GSE109037) or 25% (GSE109033) mitochondrial

93 transcript fraction were excluded to select single cells with high quality mRNA profiles. The data
94 was normalized by the total expression, scaled and log transformed. Identification of 2,000 highly
95 variable features was followed by PCA to reduce the number of dimensions representing each cell.
96 Statistically significant 15 PCs were selected based on the JackStraw and Elbow plots and provided
97 as input for constructing a K-nearest-neighbors (KNN) graph based on the Euclidean distance in
98 PCA space. Cells were clustered by the Louvain algorithm with a resolution parameter 0.1.
99 Uniform Manifold Approximation and Projection (UMAP) was used to visualize and explore
100 cluster data. Marker genes that define each cluster were identified by comparing each cluster to all
101 other clusters using the MAST (Finak et al. 2015) provided in Seurat package. In order to correct
102 batch effects among samples and experiments, we applied the Harmony package (ver.1.0)
103 (Korsunsky et al. 2019) to the datasets. The Markov Affinity-based Graph Imputation of Cells
104 (MAGIC) algorithm (ver.2.0.3) (van Dijk et al. 2018) was used to denoise and the count matrix
105 and impute the missing data. In these testis datasets from adult human, we identified 23,896 high
106 quality single cells, that were clustered into 7 major cell types, including spermatogonia,
107 spermatocytes, early spermatids, late spermatids, peritubular myoid cell, endothelial cell, and
108 macrophage. Similarly, we exploited 30,268 high quality single cells from eight adult and three 6-
109 day postpartum mouse testis tissue samples and subsequently defined 11 major cell populations.

110 **Sperm Immunocytochemistry and Free Thiol Labeling Assay**

111 Mouse and human sperm were washed in PBS twice, attached on the glass coverslips, and fixed
112 with 4% paraformaldehyde (PFA) in PBS at room temperature (RT) for 10 min (mouse) or at 4°C
113 for 1 hr (human). Fixed samples were permeabilized using 0.1% Triton X-100 in PBS at RT for
114 10 min, washed in PBS, and blocked with 10% goat serum in PBS at RT for 1 hr. Cells were
115 stained with antibody in PBS supplemented with 10% goat serum at 4°C overnight. After washing
116 in PBS, the samples were incubated with goat anti-rabbit Alexa 647 or Alexa 555-plus (Invitrogen,
117 1:1,000) in 10% goat serum in PBS at RT for 1 hr. Hoechst was used to counterstain nucleus for
118 sperm head. For BODIPY-N-ethylmaleimide labeling, reduced thiols within proteins were
119 alkylated with BODIPY FL maleimide (final concentration of 10 nM, ThermoFisher) for 30 min
120 in the dark after permeabilization. The sample was then quenched by the addition of 500 mM 2-
121 mercaptoethanol for 30 min in the dark, followed by 3 times washing in PBS. For ThiolTracker
122 (ThermoFisher) labeling, fixed sperm were stained with 20 μM dye, followed by 3 times washing
123 in PBS. Stained sperm samples were mounted with Prolong gold (Invitrogen) and cured for 24 hr,

124 followed by imaging with Zeiss LSM710 Elyra P1 using Plan-Apochrombat 63X/1.40 or alpha
125 Plan-APO 100X/1.46 oil objective lens (Carl Zeiss).

126 **Protein Extraction and Western Blotting**

127 Whole sperm protein was extracted as previously described (Chung et al. 2011, Chung et al. 2014,
128 Chung et al. 2017). In short, mouse epididymal spermatozoa washed in PBS were directly lysed
129 in 2× SDS sample buffer or 8 M urea. The whole sperm lysate was centrifuged at 15,000 g, 4°C
130 for 10 min. Supernatant were adjusted to 50 mM DTT and denatured at 95°C for 10 min before
131 loading to gel. The membranes were incubated overnight at 4°C with primary antibody, followed
132 by washing with PBST and incubation with appropriate secondary antibody for 1 hr. Bands were
133 visualized using chemiluminescence and imaged by ChemiDoc (Bio-Rad). Antibodies used for
134 Western blotting were rabbit anti-mouse TXNRD3 (1:2000), GPx4 (1:2000), ANT4, 1 μg/mL;
135 P2X2, 1 μg/mL; TOM20, 0.2 μg/mL; TXNRD1, 1 μg/mL; TXNRD2, 1 μg/mL; acetylated tubulin
136 and anti-acetylated tubulin (1: 20,000). Secondary antibodies were anti-rabbit IgG-HRP (1:10,000)
137 and anti-mouse IgG-HRP (1:10,000) from Jackson ImmunoResearch (West Grove, PA).

138 **Protein Oxidation**

139 Carbonyl groups inserted into proteins by oxidative reactions were evaluated with protein carbonyl
140 assay kit (Abcam). Briefly, samples were homogenized and processed according to the
141 manufacturer's protocol. The carbonyl groups in the solubilized protein samples were derivatized
142 using DNPH (2, 4 dinitrophenyl hydrazine) or control solution for 15 min and then neutralized.
143 The samples were then loaded onto SDS PAGE gels and DNP conjugated proteins were detected
144 by western blotting using primary DNP antibody and HRP conjugated secondary antibody.

145 **Flagella Waveform Analysis**

146 To tether sperm head for planar beating, non-capacitated or capacitated spermatozoa (2-3×10^5 cells)
147 from adult male mice were transferred to the fibronectin-coated 37°C chamber for Delta T culture
148 dish controller (Bioptechs) filled with HS and HEPES-buffered HTF medium (H-HTF)(Chung et
149 al. 2017), respectively. Flagellar movements of the tethered sperm were recorded for 2 s with 200
150 fps using pco.edge sCMOS camera equipped in Axio observer Z1 microscope (Carl Zeiss). All
151 movies were taken at 37°C within 10 min after transferring sperm to the imaging dish. FIJI
152 software (Schindelin et al. 2012) was used to measure beating frequency of sperm tail, and to
153 generate overlaid images to trace waveform of sperm flagella as previously described (Chung et
154 al. 2017).

155 **Sperm Motility Analysis**

156 Aliquots of sperm were placed in slide chamber (CellVision, 20 mm depth) and motility was
157 examined on a 37°C stage of a Nikon E200 microscope under 10X phase contrast objective (CFI
158 Plan Achro 10X/0.25 Ph1 BM, Nikon). Images were recorded (40 frames at 50 fps) using CMOS
159 video camera (Basler acA1300-200um, Basler AG, Ahrensburg, Germany) and analyzed by
160 computer-assisted sperm analysis (CASA, Sperm Class Analyzer version 6.3, Microptic,
161 Barcelona, Spain). Sperm total motility and hyperactivated motility was quantified simultaneously.
162 Over 200 motile sperm were analyzed for each trial, at least 3 biological replicates were performed
163 for each genotype. To track swimming trajectory, the sperm motility was videotaped at 50 fps. The
164 images were analyzed using Fiji software (Schindelin et al. 2012) by assembling overlays of the
165 flagellar traces generated by hyperstacking binary images of 20 frames of 2 s movies coded in a
166 gray intensity scale.

167 **Scanning Electron Microscopy**

168 Sperm cells were attached on the glass coverslips and fixed with 2.5% glutaraldehyde (GA) in 0.1
169 M sodium cacodylate buffer (pH 7.4) for one hour at 4°C and post fixed in 2% osmium tetroxide
170 in 0.1 M cacodylate buffer (pH 7.4). The fixed samples were washed with 0.1 M cacodylate buffer
171 for 3 times and dehydrated through a series of ethanol to 100%. The samples were dried using a
172 300 critical point dryer with liquid carbon dioxide as transitional fluid. The coverslips with dried
173 samples were glued to aluminum stubs and sputter coated with 5 nm platinum using a Cressington
174 208HR (Ted Pella) rotary sputter coater. Prepared samples were imaged with Hitachi SU-70
175 scanning electron microscope (Hitachi High-Technologies).

176 **Transmitted Electron Microscopy**

177 Collected epididymal sperm cells were washed and pelleted by centrifugation and fixed in 2.5%
178 GA and 2% PFA in 0.1 M cacodylate buffer pH 7.4 for one hour at RT. Fixed sperm pellets were
179 rinsed with 0.1 M cacodylate buffer and spud down in 2% agar. The chilled blocks were trimmed,
180 rinsed in the 0.1 M cacodylate buffer, and replaced with 0.1% tannic acid in the buffer for one
181 hour. After rinsing in the buffer, the samples were post-fixed in 1% osmium tetroxide and 1.5%
182 potassium ferrocyanide in 0.1 M cacodylate buffer for one hour. The post-fixed samples were
183 rinsed in the cacodylate buffer and distilled water, followed by en bloc staining in 2% aqueous
184 uranyl acetate for one hour. Prepared samples were rinsed and dehydrated in an ethanol series to
185 100%. Dehydrated samples were infiltrated with epoxy resin Embed 812 (Electron Microscopy

186 Sciences), placed in silicone molds and baked for 24 hours at 60°C. The hardened blocks were
187 sectioned in 60 nm thickness using Leica UltraCut UC7. The sections were collected on grids
188 coated with formvar/carbon and contrast stained using 2% uranyl acetate and lead citrate. The
189 grids were imaged using FEI TecnaiBiotwin Transmission Electron Microscope (FEI, Hillsbroro,
190 OR) at 80 kV. Images were taken using MORADA CCD camera and iTEM (Olympus) software.

191 **Sperm Chromatin Dispersion Test (Halo Assay)**

192 Samples were diluted to the concentration of 5-10×10^6 cells/mL, then mixed with low-melting-
193 point aqueous agarose to obtain a final concentration of 0.7% agarose. 50 µl mixture was dispensed
194 onto a glass slide pre-coated with 0.65% standard agarose, then covered by a coverslip for
195 solidification at 4°C for 4 min. The coverslip was then removed carefully before the sample was
196 immersed into freshly prepared acid denaturation solution (0.08 N HCl) for 7 min, neutralizing
197 and lysing solution 1 (0.4 M Tris-HCl, 0.8M DTT, 1% SDS, 50 mM EDTA, pH 7.5) for 10 min,
198 and neutralizing and lysing solution 2 (0.4 M Tris-HCl, 2 M NaCl, 1% SDS, pH 7.5) for 5 min at
199 RT in sequence. The slide was then transferred to Tris-borate EDTA solution (90 mM Tris-borate,
200 2 mM EDTA, pH 7.5) for 2 min, then dehydrated in sequential 70%, 90%, and 100% EtOH (2 min
201 each). After drying, the slide was stained with DAPI (2 ug/ml), then examined under microscope
202 as described above. The Halo size (diameter) was defined and classified into big (>17 µm),
203 medium (between 12 and 17 µm) and small size (<12 µm).

204 **Acridine Orange Assay**

205 Sperm cells were smeared on glass slide until dry, followed by washing in PBS pH 7.2. 4%
206 paraformaldehyde (PFA) was used to fix cells for 15 min at RT, then covered by methanol for 5
207 min. washed with PBS for 5 min. The sample was incubated in RNAse A solution at 37°C for 30
208 min. Washing with PBS of pH 7.2 for 5 min was performed between each step. 0.1 M HCl was
209 used for DNA denaturation for 30-45 sec, followed by AO staining working solution for 2 min.
210 The slide was ready for examination under fluorescence microscopy after washing gently and
211 drying.

212 **Mitochondrial Membrane Potential ($\Delta\Psi m$) Measurement**

213 Epididymal sperm were attached on Delta T culture chamber coated with poly-D-Lysine (2 mg/mL)
214 or together with Cell-Tak for 30 min. Unattached sperm were removed by the gentle pipette wash.
215 Mitotracker deep red (working concentration 500 nM, ThermoFisher) was loaded in sperm for 30
216 min, followed by gentle rinse with HS or HEPES-buffered HTF medium H-HTF. All movies were

217 taken at 37°C by the pco.edge sCMOS camera equipped in Axio observer Z1 microscope (Carl
218 Zeiss). The data were analyzed by Zen (Blue).

219 **Quantification and Statistical Analysis**

220 Statistical analyses were performed using Student's t-test or one-way analysis of variance
221 (ANOVA) with Tukey post hoc test. Differences were considered significant at $*p < 0.05$, $**p <$
222 0.01, and $***p < 0.001$.

223 **Results**

224 ***Txnrd3*$^{-/-}$ Sperm Cells Display Defects in Morphology and Motility Under Capacitating Conditions**

225 To understand why *Txnrd3*$^{-/-}$ males exhibit sub-fertility *in vivo* and *in vitro* (Dou et al., 2021), we
226 first examined sperm morphology and count from the cauda epididymis. The number of sperm
227 produced by *Txnrd3*$^{-/-}$ males was smaller than that from 2-3 months old heterozygous littermates
228 (Supplementary Figure 1A). Among them, some *Txnrd3*$^{-/-}$ sperm displayed hairpin formation
229 within midpiece, specifically evident after 90 min incubation under capacitating conditions (Figure
230 1A, B), whereas sperm bent around annulus were negligible in both wild type and *Txnrd3*$^{-/-}$ mice.
231 Scanning electron microscopy (SEM) analysis did not reveal any gross abnormalities in the sperm
232 midpiece (Figure 1C).

233

234 Prompted by the observation of capacitation-associated hairpin formation within midpiece of
235 *Txnrd3*$^{-/-}$ sperm, we next analyzed sperm motility. Flagellar waveform analysis revealed that
236 *Txnrd3*$^{-/-}$ sperm become stiff in the midpiece and beat abnormally after incubating under
237 capacitating conditions (Figure 1D, Supplementary Figure 1C and Video S1). Accordingly, CASA
238 analysis found that overall motility of *Txnrd3*$^{-/-}$ sperm was diminished (Supplementary Figure 1B).
239 By contrast, hyperactivated motility was not significantly affected, likely because the *Txnrd3*$^{-/-}$
240 sperm that are not bent still developed hyperactivated motility. To better understand the effect of
241 TXNRD3 deficiency on free swimming pattern, sperm cells were placed in 0.3% methylcellulose
242 which mimics viscous environment in the female reproductive tract. Swimming trajectory traced
243 by time-lapse video microscope demonstrated that *Txnrd3*$^{-/-}$ sperm move a shorter distance at a
244 given time after capacitation (Figure 1E and Video S2), suggesting that the hairpin prevents them
245 from swimming as efficiently as wild type sperm.

246

247 **Absence of TXNRD3 Affects the Redox State of Both Head and Tail of Sperm**

248 TXNRD3 is enriched in the testis but not readily detected in the epididymis (Su et al. 2005). Our
249 analysis of the publicly available scRNA-seq dataset (Speir et al. 2020) found that *Txrnd3* mRNA
250 expression is high in spermatogonia and spermatocytes and reduced in spermatids (Supplementary
251 Figure 2). We hypothesized that diminishing TXNRD3 mRNA and protein levels in epididymal
252 sperm along the tract underlies the changes in the overall redox state of proteins during epididymal
253 maturation and capacitation of sperm. Thus, we examined changes in TXNRD3 protein levels and
254 found decreasing amount of TXNRD3 in sperm during their descent through epididymis (Figure
255 2A, B). We next examined the distribution and the extent of protein thiol modification in the
256 absence of TXNRD3 by labeling epididymal sperm cells with ThiolTracker that reacts with
257 reduced thiols (free "-SH") irreversibly. Consistent with TXNRD3 levels from caput to cauda,
258 wild type sperm from caput region exhibited strong fluorescence over the entire cell whereas
259 corpus and cauda sperm displayed gradually diminishing fluorescence intensity, more noticeably
260 in the head (Figure 2C, D). These results are in line with the previously reported increasing
261 disulfide bond formation in sperm during their transit along the male reproductive tract (Dias et al.
262 2014).
263
264 Using ThiolTracker or BODIPY-NEM, another thiol-reactive dye, we found that, in the absence
265 of TXNRD3, free thiol content is further decreased modestly, yet significantly, in cauda sperm
266 (Figure 2C, D and Supplementary Figure 3A). It is possible that other reductases function
267 redundantly and compensate for the loss of TXNRD3; e.g. both TXNRD1 and TXNRD2 proteins
268 are detected in wild type and *Txnrd3*$^{-/-}$ sperm (Supplementary Figure 3D), and there are other thiol
269 oxidoreductases, including those specific to the male reproductive system, that are also expressed.
270 As sperm proteins were found more oxidized in cauda than in caput, we speculate that the
271 efficiency of protein extraction can be affected by the overall redox status. Indeed, when we used
272 urea instead of SDS to examine protein levels of TXNRD3 from caput, corpus, and cauda sperm,
273 we did not observe significant difference (Figure 2E), suggesting that TXNRD3 itself is likely a
274 substrate of thioredoxin system during epididymal maturation.
275
276 Sperm midpiece harbors compartmentalized mitochondria (Skinner 2018) (see also Figure 1C).
277 As *Txnrd3*$^{-/-}$ sperm specifically exhibit the hairpin formation within the midpiece, next we tested
278 whether the TXNRD3 loss-of-function affects the redox states of mitochondrial proteins more

279 specifically. In the SDS extracted fraction, the protein level of glutathione peroxidase 4 (GPX4) -
280 a mitochondrial structural protein and potential substrate of TXNRD3 (Ursini et al. 1999, Su et al.
281 2005) – was much lower in the cauda sperm just as seen for TXNRD3 (Figure 2A, B and
282 Supplementary Figure 3B,C). By contrast, urea readily extracted GPx4 even from cauda sperm
283 (Figure 2F, *supernatant*), indicating that GPx4 becomes likely more oxidized and therefore SDS-
284 insoluble during epididymal transit. Intriguingly, we observed a urea-insoluble GPx4 fraction not
285 in wild type but in *Txnrd3*$^{-/-}$ cauda sperm when the pellet was further solubilized by guanidine
286 following urea treatment (Figure 2F, *pellet*). Other non-structural but membrane proteins localized
287 in sperm mitochondria or midpiece such as ANT4, P2X2 and TOM20 and the other two
288 thioredoxin reductases - TXNRD1 and TXNRD2 - were well solubilized in all detergents tested
289 (Figure 2F and Supplementary Figure 3D). Taken together, our data clearly showed that TXNRD3
290 is involved in redox regulation of sperm proteins during epididymal transition.
291
292 **Capacitation-Associated Oxidation is Deregulated in *Txnrd3*$^{-/-}$ Sperm (Chromatin Organization)**
293 It has been known that redox signaling is involved in sperm capacitation (O'Flaherty 2015). We
294 next examined how free thiol levels change during sperm capacitation. Under capacitating
295 conditions, wild type sperm were less reactive with ThiolTracker, particularly in the head, whereas
296 *Txnrd3*$^{-/-}$ sperm was not reactive regardless (Figure 3A). These results suggest that sperm proteins
297 were more oxidized in the absence of TXNRD3 during sperm maturation, which remain relatively
298 stable during capacitation. To test this idea, we examined protein oxidation levels by detecting
299 carbonyl groups inserted into proteins. Incubating sperm under capacitating conditions
300 dramatically increased sperm protein carbonylation, suggesting active oxidative reactions occur.
301 The protein oxidation level was further enhanced in *Txnrd3*$^{-/-}$ sperm (Figure 3B and Supplementary
302 Figure 4).
303
304 As the free thiol level changes were most dramatic in the head, we next investigated the loss of
305 TXNRD3 function on sperm chromatin organization. We examined the extent of DNA integrity
306 by halo assay where radial dispersion of the DNA fragments from the nucleus was measured upon
307 artificial acid denaturation; the bigger the halo size is, the less damaged DNA fragment is present
308 (Fernández et al. 2003, Chohan et al. 2006, Tandara et al. 2014). Intriguingly, *Txnrd3*$^{-/-}$ sperm resist
309 the denaturation better, developing smaller halos than those of wild type sperm (Figure 4). This

310 result suggests that more damaged, double stranded DNA fragments are present in the nucleus in
311 the absence of TXNRD3, likely due to more DNA fragments crosslinked to proteins. The nuclei
312 of sperm incubated under capacitating conditions, developed smaller halos in both wild type and
313 *Txnrd3*$^{-/-}$ sperm (Figure 4). We further evaluated the altered resistance of DNA to acid denaturation
314 by acridine orange (AO) assay; AO produces different emission when bound to single vs. double
315 stranded DNA. We observed that double-stranded DNA was more stable and resistant to acid
316 denaturation in both nucleus and mitochondria in capacitated *Txnrd3*$^{-/-}$ sperm (Supplementary
317 Figure 5). Taken together, the thiol oxidoreductase function is diminished in *Txnrd3*$^{-/-}$ sperm
318 compared to wild type sperm. The data show that TXNRD3 supports redox regulation of
319 epididymal sperm maturation, protecting mitochondrial structure and chromatin from oxidative
320 damage during sperm capacitation.
321
322 **Lack of TXNRD3 Dysregulates Capacitation-Induced Remodeling of Sperm Mitochondrial**
323 **Ultrastructure**
324 To maintain motility and support capacitation after ejaculation, mammalian sperm utilize
325 nutrient molecules in the seminal plasma and in the female reproductive tract environment to
326 generate energy (Visconti 2012). As terminally differentiated and highly polarized cells, sperm
327 uniquely compartmentalize metabolic pathways in the flagella: the glycolytic enzymes are
328 specifically localized in the principal piece, whereas mitochondrial oxidative phosphorylation
329 (OXPHOS) occurs in the midpiece (Skinner 2018). A classic view on mouse sperm bioenergetics
330 has been that glycolysis is the main metabolic pathway to support tyrosine phosphorylation and
331 hyperactivation whereas both glycolytic and OXPHOS are functional (Travis et al. 2001, Mukai
332 and Okuno 2004, Goodson et al. 2012). Intriguingly, our transmission electron microscopy
333 (TEM) analysis revealed that mitochondria display more well-defined cristae after incubating
334 under capacitating conditions (Figure 5A, B). Dimerization of the V-like shaped mitochondrial
335 ATPase and its self-assembly into rows drives the cristae organization and determines respiratory
336 efficiency (Dudkina et al. 2006, Strauss et al. 2008, Cogliati et al. 2013, Blum et al. 2019). Thus,
337 our results suggest that capacitation increases mitochondrial activity in mouse sperm. In addition,
338 we observed that capacitation induces electron-dense cores in the mitochondrial matrix of
339 capacitated sperm cells (Figure 5A, B). Notably, *Txnrd3*$^{-/-}$ sperm developed significantly more
340 dense cores than wild type sperm regardless of capacitation status. As similar dense cores were

341 previously reported in *Pmca4*$^{-/-}$ sperm that might potentially experience Ca^{2+} overload (Okunade
342 et al. 2004), this result suggests that the TXNRD3-dependent redox control might impact on
343 Ca^{2+} signaling during sperm capacitation.
344

345 ***Txnrd3*$^{-/-}$ Sperm Lose Control of Mitochondrial Membrane Hyperpolarization**

346 Mitochondrial membrane potential (ΔΨm) is an essential driving force for oxidative
347 phosphorylation. To better understand how mitochondrial activity changes during sperm
348 capacitation and the loss-of-function effect of TXNRD3 on this process, we performed functional
349 imaging to probe ΔΨm using MitoTracker DeepRed, a fluorescent dye specifically taken up by
350 mitochondria in live cells according to ΔΨm (Lugli et al. 2005, Zhou et al. 2011, Greene et al.
351 2012). The decreased fluorescence intensity of MitoTracker DeepRed indicates mitochondrial
352 depolarization. In agreement with the higher mitochondrial activity during capacitation, dissipated
353 ΔΨm by antimycin A - an inhibitor of oxidative phosphorylation - was greater in wild type sperm
354 incubated under capacitating conditions (Figure 6 and Supplementary Figure 6). Under non-
355 capacitating conditions, we find that ΔΨm is not significantly different between wild type and
356 *Txnrd3*$^{-/-}$ sperm. Under capacitating conditions, however, we found two distinct populations among
357 TXNRD3-deficient sperm in terms of ΔΨm (Figure 6 and Supplementary Figure 6); one group did
358 not show any change in the fluorescent intensity of the dye upon antimycin A, suggesting reduced
359 or no mitochondrial activity (red trace) whereas the other group exhibited ΔΨm at a similar level
360 to that of wild type sperm. These results further show that the loss of TXNRD3 dysregulates the
361 capacitation-associated remodeling of mitochondrial function in mouse sperm.

362 **Discussion**

363 **Evidence that TXNRD3 Supports Sperm Function and Redox Regulation in Male Fertility**

364 In the accompanying manuscript, we show that *Txnrd3*$^{-/-}$ male mice exhibit reduced fertility *in vivo*
365 and *in vitro* (Dou et al., 2021). The findings in this study demonstrate that the subfertility likely
366 results from the combinatorial effects of defective chromatin organization and capacitation-
367 induced tail bending within the midpiece. The high degree of sperm DNA fragmentation was
368 reported to correlate with low fertilization rates, embryo quality and pregnancy after IVF and
369 intracytoplasmic sperm injection (Loft et al. 2003, Tandara et al. 2014). The bent tail would force
370 the head backwards, opposite to the swimming direction of the sperm. Additionally, TXNRD3 in

371 sperm is gradually oxidized during epididymal transit, which is consistent with reduced free thiol
372 group levels in cells along the epididymal tract. Therefore, the main timing of TXNRD3 function
373 is during spermatogenesis in the testis and epididymal maturation rather than the subsequent
374 fertilization process. Moderate changes in the free thiol levels and redox status of the *Txnrd3*$^{-/-}$
375 sperm may be due to functional redundancy of other thiol reductases that partly compensate for
376 the loss of TXNRD3. The data are also consistent with the mode wherein TXNRD3 supports
377 accelerated redox remodeling during sperm maturation, which may also occur, albeit at a lower
378 rate, in the absence of this enzyme. Alternatively, the overall redox status is only marginally
379 changed in the absence of TXNRD3, but the pattern of disulfide bond formation could be jumbled,
380 sufficient to make *Txnrd3*$^{-/-}$ sperm vulnerable to capacitation-associated oxidative damage.
381
382 **Mitochondrial Function and Control of Metabolism During Capacitation**
383 Mitochondria is a key organelle still preserved in the fully differentiated spermatozoa. Previous
384 knock-out studies of sperm-specific glyceraldehyde 3-phosphate dehydrogenase and
385 phosphoglycerate kinase 2 have identified glycolysis as the main source of ATP to sustain the
386 motility of mouse spermatozoa (Miki et al. 2004, Danshina et al. 2010). Because OXPHOS yields
387 more ATP per mol of glucose than glycolysis, the discordant contribution of the two metabolic
388 pathways to provide the energy for mouse sperm motility has been an unresolved puzzle for a long
389 time. A comparative study revealed that sperm of closely related mouse species with higher oxygen
390 consumption rate were able to produce higher amounts of ATP, achieving higher swimming
391 velocities (Tourmente et al. 2015).
392
393 Here we report, to our knowledge for the first time, that capacitation induces sperm mitochondria
394 to form more defined cristae (Figure 5). As ATPase dimerization and self-assembly drive cristae
395 formation (Dudkina et al. 2006, Strauss et al. 2008, Blum et al. 2019), this result indicates that
396 capacitation enhances OXPHOS pathway to supply additional ATP. The higher metabolic activity
397 in capacitating sperm is further supported by our observation of a more hyperpolarized
398 mitochondrial membrane potential ($\Delta\Psi m$) (Figure 6), an indication of protonmotive force and
399 mitochondrial function. Consistently, a recent study reported accelerated oxygen consumption rate
400 in capacitated sperm (Balbach et al. 2020).
401

402 Interestingly, we observed that a significant portion of TXNRD3-deficient sperm do not only fail
403 to maintain ΔΨm but also develop a more apparent electron-dense core in the mitochondrial matrix.
404 As a condensed mitochondrial matrix was observed in the absence of plasma membrane Ca^{2+}-
405 ATPase 4 (Okunade et al. 2004), this result suggests that calcium is overloaded in *Txnrd3*$^{-/-}$ sperm
406 mitochondria during sperm capacitation. Whether the TXNRD3-deficient sperm cells that cannot
407 maintain ΔΨm are the same sperm populations with the electron-dense core requires further work.
408 The small cytosol volume in mature sperm makes it difficult to achieve spatial resolution specific
409 to mitochondria Ca^{2+} imaging with the currently available Ca^{2+} dyes. Generation of a mouse model
410 expressing a genetically encoded Ca^{2+} indicator specifically targeted to sperm mitochondria will
411 help to directly address the functional relationship of redox regulation of mitochondria dynamics
412 in Ca^{2+} homeostasis and sperm metabolism during capacitation.
413
414 In summary, our study investigated the TXNRD3 function and potential cellular mechanisms in
415 sperm maturation and male fertility. The absence of TXNRD3 deregulates the redox control of
416 sperm chromatin and mitochondrial structure proteins during capacitation, resulting in distinct
417 hairpin-like bending and defective mitochondrial respiration; the loss-of-function prevents *Txnrd3*$^{-}$
418 $^{/-}$ sperm from properly positioning to penetrate the egg, compromising efficient ATP production.
419 *Txnrd3*$^{-/-}$ mice are fertile in controlled laboratory environment without limitation of resource and
420 male competition. Yet our findings from *in vitro* experiments show that TXNRD3 and the
421 thioredoxin system intimately contribute to sperm function and male reproduction. This new
422 knowledge could help to define conditions for assisted reproductive technology in clinic.

423 **Conflict of Interest**

424 The authors declare no competing interests.

425 **Author Contributions**

426 J.-J.C. and V.N.G. conceived the study. J.-J.C. oversaw the project. J.-J.C. and H.W. designed the
427 experiments. H.W., Q.D., and J.-J.C. performed experiments. K.J. and J.C. analyzed scRNAseq
428 database. H.W. prepared the figures and H.W. and J.-J.C wrote the initial draft of the manuscript.
429 H.W., V.N.G. and J.-J.C. edited the manuscript with input from all other authors in the final version.

430 **Funding**

This work was funded by NIH R01GM065204 to V.N.G, and the start-up funds from Yale School of Medicine and NIH R01HD096745 to J.-J.C.

Acknowledgments

We thank the Harvard Medical School EM facility (TEM) and the Yale Center for Cellular and Molecular Imaging (SEM) for assistance in electron microscopy, Jae Yeon Hwang for help in analyzing TEM images of sperm mitochondria, and Xiaofang Huang for initial analysis of free thiol measurement.

Reference

Arnér, E. S. and A. Holmgren (2000). "Physiological functions of thioredoxin and thioredoxin reductase." Eur J Biochem **267**(20): 6102-6109.

Balbach, M., M. G. Gervasi, D. M. Hidalgo, P. E. Visconti, L. R. Levin and J. Buck (2020). "Metabolic changes in mouse sperm during capacitation†." Biol Reprod **103**(4): 791-801.

Blum, T. B., A. Hahn, T. Meier, K. M. Davies and W. Kühlbrandt (2019). "Dimers of mitochondrial ATP synthase induce membrane curvature and self-assemble into rows." Proc Natl Acad Sci U S A **116**(10): 4250-4255.

Chabory, E., C. Damon, A. Lenoir, G. Kauselmann, H. Kern, B. Zevnik, C. Garrel, F. Saez, R. Cadet, J. Henry-Berger, M. Schoor, U. Gottwald, U. Habenicht, J. R. Drevet and P. Vernet (2009). "Epididymis seleno-independent glutathione peroxidase 5 maintains sperm DNA integrity in mice." J Clin Invest **119**(7): 2074-2085.

Chohan, K. R., J. T. Griffin, M. Lafromboise, C. J. De Jonge and D. T. Carrell (2006). "Comparison of chromatin assays for DNA fragmentation evaluation in human sperm." J Androl **27**(1): 53-59.

Chung, J. J., K. Miki, D. Kim, S. H. Shim, H. F. Shi, J. Y. Hwang, X. Cai, Y. Iseri, X. Zhuang and D. E. Clapham (2017). "CatSperζ regulates the structural continuity of sperm Ca(2+) signaling domains and is required for normal fertility." Elife **6**.

Chung, J. J., B. Navarro, G. Krapivinsky, L. Krapivinsky and D. E. Clapham (2011). "A novel gene required for male fertility and functional CATSPER channel formation in spermatozoa." Nat Commun **2**: 153.

Chung, J. J., S. H. Shim, R. A. Everley, S. P. Gygi, X. Zhuang and D. E. Clapham (2014). "Structurally distinct Ca(2+) signaling domains of sperm flagella orchestrate tyrosine phosphorylation and motility." Cell **157**(4): 808-822.

Cogliati, S., C. Frezza, M. E. Soriano, T. Varanita, R. Quintana-Cabrera, M. Corrado, S. Cipolat, V. Costa, A. Casarin, L. C. Gomes, E. Perales-Clemente, L. Salviati, P. Fernandez-Silva, J. A. Enriquez and L. Scorrano (2013). "Mitochondrial cristae shape determines respiratory chain supercomplexes assembly and respiratory efficiency." Cell **155**(1): 160-171.

Conrad, M., C. Jakupoglu, S. G. Moreno, S. Lippl, A. Banjac, M. Schneider, H. Beck, A. K. Hatzopoulos, U. Just, F. Sinowatz, W. Schmahl, K. R. Chien, W. Wurst, G. W. Bornkamm and M. Brielmeier (2004). "Essential role for mitochondrial thioredoxin reductase in hematopoiesis, heart development, and heart function." Mol Cell Biol **24**(21): 9414-9423.

Danshina, P. V., C. B. Geyer, Q. Dai, E. H. Goulding, W. D. Willis, G. B. Kitto, J. R. McCarrey, E. M. Eddy and D. A. O'Brien (2010). "Phosphoglycerate kinase 2 (PGK2) is essential for sperm function and male fertility in mice." Biol Reprod **82**(1): 136-145.

de Lamirande, E., H. Jiang, A. Zini, H. Kodama and C. Gagnon (1997). "Reactive oxygen species and sperm physiology." Rev Reprod **2**(1): 48-54.

Dias, G. M., M. L. López, A. T. Ferreira, D. A. Chapeaurouge, A. Rodrigues, J. Perales and C. A. Retamal (2014). "Thiol-disulfide proteins of stallion epididymal spermatozoa." Anim Reprod Sci **145**(1-2): 29-39.
Dou, Q., ..Hwang, J.Y., … Chung, J.-J. Gladyshev, V.N. (2021) "Title TBD" to be posted to bioRxiv
Dudkina, N. V., S. Sunderhaus, H. P. Braun and E. J. Boekema (2006). "Characterization of dimeric ATP synthase and cristae membrane ultrastructure from Saccharomyces and Polytomella mitochondria." FEBS Lett **580**(14): 3427-3432.
Fernández, J. L., L. Muriel, M. T. Rivero, V. Goyanes, R. Vazquez and J. G. Alvarez (2003). "The sperm chromatin dispersion test: a simple method for the determination of sperm DNA fragmentation." J Androl **24**(1): 59-66.
Finak, G., A. McDavid, M. Yajima, J. Deng, V. Gersuk, A. K. Shalek, C. K. Slichter, H. W. Miller, M. J. McElrath, M. Prlic, P. S. Linsley and R. Gottardo (2015). "MAST: a flexible statistical framework for assessing transcriptional changes and characterizing heterogeneity in single-cell RNA sequencing data." Genome Biol **16**: 278.
Gervasi, M. G. and P. E. Visconti (2017). "Molecular changes and signaling events occurring in spermatozoa during epididymal maturation." Andrology **5**(2): 204-218.
Goodson, S. G., Y. Qiu, K. A. Sutton, G. Xie, W. Jia and D. A. O'Brien (2012). "Metabolic substrates exhibit differential effects on functional parameters of mouse sperm capacitation." Biol Reprod **87**(3): 75.
Greene, A. W., K. Grenier, M. A. Aguileta, S. Muise, R. Farazifard, M. E. Haque, H. M. McBride, D. S. Park and E. A. Fon (2012). "Mitochondrial processing peptidase regulates PINK1 processing, import and Parkin recruitment." EMBO Rep **13**(4): 378-385.
Henkel, R., E. Kierspel, T. Stalf, C. Mehnert, R. Menkveld, H. R. Tinneberg, W. B. Schill and T. F. Kruger (2005). "Effect of reactive oxygen species produced by spermatozoa and leukocytes on sperm functions in non-leukocytospermic patients." Fertil Steril **83**(3): 635-642.
Hermann, B. P., K. Cheng, A. Singh, L. Roa-De La Cruz, K. N. Mutoji, I. C. Chen, H. Gildersleeve, J. D. Lehle, M. Mayo, B. Westernstroer, N. C. Law, M. J. Oatley, E. K. Velte, B. A. Niedenberger, D. Fritze, S. Silber, C. B. Geyer, J. M. Oatley and J. R. McCarrey (2018). "The Mammalian Spermatogenesis Single-Cell Transcriptome, from Spermatogonial Stem Cells to Spermatids." Cell Rep **25**(6): 1650-1667 e1658.
Holmgren, A. (1980). "Pyridine nucleotide - disulfide oxidoreductases." Experientia Suppl **36**: 149-180.
Jakupoglu, C., G. K. Przemeck, M. Schneider, S. G. Moreno, N. Mayr, A. K. Hatzopoulos, M. H. de Angelis, W. Wurst, G. W. Bornkamm, M. Brielmeier and M. Conrad (2005). "Cytoplasmic thioredoxin reductase is essential for embryogenesis but dispensable for cardiac development." Mol Cell Biol **25**(5): 1980-1988.
Kao, S. H., H. T. Chao, H. W. Chen, T. I. S. Hwang, T. L. Liao and Y. H. Wei (2008). "Increase of oxidative stress in human sperm with lower motility." Fertil Steril **89**(5): 1183-1190.
Korsunsky, I., N. Millard, J. Fan, K. Slowikowski, F. Zhang, K. Wei, Y. Baglaenko, M. Brenner, P. R. Loh and S. Raychaudhuri (2019). "Fast, sensitive and accurate integration of single-cell data with Harmony." Nat Methods **16**(12): 1289-1296.
Loft, S., T. Kold-Jensen, N. H. Hjollund, A. Giwercman, J. Gyllemborg, E. Ernst, J. Olsen, T. Scheike, H. E. Poulsen and J. P. Bonde (2003). "Oxidative DNA damage in human sperm influences time to pregnancy." Hum Reprod **18**(6): 1265-1272.
Lugli, E., L. Troiano, R. Ferraresi, E. Roat, N. Prada, M. Nasi, M. Pinti, E. L. Cooper and A. Cossarizza (2005). "Characterization of cells with different mitochondrial membrane potential during apoptosis." Cytometry A **68**(1): 28-35.
Miki, K., W. Qu, E. H. Goulding, W. D. Willis, D. O. Bunch, L. F. Strader, S. D. Perreault, E. M. Eddy and D. A. O'Brien (2004). "Glyceraldehyde 3-phosphate dehydrogenase-S, a sperm-specific glycolytic enzyme, is required for sperm motility and male fertility." Proc Natl Acad Sci U S A **101**(47): 16501-16506.
Mukai, C. and M. Okuno (2004). "Glycolysis plays a major role for adenosine triphosphate supplementation in mouse sperm flagellar movement." Biol Reprod **71**(2): 540-547.
Mustacich, D. and G. Powis (2000). "Thioredoxin reductase." Biochem J **346 Pt 1**(Pt 1): 1-8.

521 Nalvarte, I., A. E. Damdimopoulos, C. Nystöm, T. Nordman, A. Miranda-Vizuete, J. M. Olsson, L. Eriksson,
522 M. Björnstedt, E. S. Arnér and G. Spyrou (2004). "Overexpression of enzymatically active human cytosolic
523 and mitochondrial thioredoxin reductase in HEK-293 cells. Effect on cell growth and differentiation." J Biol
524 Chem **279**(52): 54510-54517.
525 O'Flaherty, C. (2015). "Redox regulation of mammalian sperm capacitation." Asian J Androl **17**(4): 583-
526 590.
527 Okunade, G. W., M. L. Miller, G. J. Pyne, R. L. Sutliff, K. T. O'Connor, J. C. Neumann, A. Andringa, D. A.
528 Miller, V. Prasad, T. Doetschman, R. J. Paul and G. E. Shull (2004). "Targeted ablation of plasma membrane
529 Ca2+-ATPase (PMCA) 1 and 4 indicates a major housekeeping function for PMCA1 and a critical role in
530 hyperactivated sperm motility and male fertility for PMCA4." J Biol Chem **279**(32): 33742-33750.
531 Schindelin, J., I. Arganda-Carreras, E. Frise, V. Kaynig, M. Longair, T. Pietzsch, S. Preibisch, C. Rueden, S.
532 Saalfeld, B. Schmid, J. Y. Tinevez, D. J. White, V. Hartenstein, K. Eliceiri, P. Tomancak and A. Cardona (2012).
533 "Fiji: an open-source platform for biological-image analysis." Nat Methods **9**(7): 676-682.
534 Skinner, M. K. (2018). Encyclopedia of Reproduction, Elsevier Science.
535 Speir, M. L., A. Bhaduri, N. S. Markov, P. Moreno, T. J. Nowakowski, I. Papatheodorou, A. A. Pollen, L.
536 Seninge, W. J. Kent and M. Haeussler (2020). "UCSC Cell Browser: Visualize Your Single-Cell Data." bioRxiv:
537 2020.2010.2030.361162.
538 Strauss, M., G. Hofhaus, R. R. Schröder and W. Kühlbrandt (2008). "Dimer ribbons of ATP synthase shape
539 the inner mitochondrial membrane." Embo j **27**(7): 1154-1160.
540 Stuart, T., A. Butler, P. Hoffman, C. Hafemeister, E. Papalexi, W. M. Mauck, 3rd, Y. Hao, M. Stoeckius, P.
541 Smibert and R. Satija (2019). "Comprehensive Integration of Single-Cell Data." Cell **177**(7): 1888-1902
542 e1821.
543 Su, D., S. V. Novoselov, Q. A. Sun, M. E. Moustafa, Y. Zhou, R. Oko, D. L. Hatfield and V. N. Gladyshev (2005).
544 "Mammalian selenoprotein thioredoxin-glutathione reductase. Roles in disulfide bond formation and
545 sperm maturation." J Biol Chem **280**(28): 26491-26498.
546 Sullivan, R. and R. Mieusset (2016). "The human epididymis: its function in sperm maturation." Hum
547 Reprod Update **22**(5): 574-587.
548 Sun, Q. A., L. Kirnarsky, S. Sherman and V. N. Gladyshev (2001). "Selenoprotein oxidoreductase with
549 specificity for thioredoxin and glutathione systems." Proc Natl Acad Sci U S A **98**(7): 3673-3678.
550 Sun, Q. A., Y. Wu, F. Zappacosta, K. T. Jeang, B. J. Lee, D. L. Hatfield and V. N. Gladyshev (1999). "Redox
551 regulation of cell signaling by selenocysteine in mammalian thioredoxin reductases." J Biol Chem **274**(35):
552 24522-24530.
553 Tandara, M., A. Bajić, L. Tandara, L. Bilić-Zulle, M. Šunj, V. Kozina, T. Goluža and M. Jukić (2014). "Sperm
554 DNA integrity testing: big halo is a good predictor of embryo quality and pregnancy after conventional
555 IVF." Andrology **2**(5): 678-686.
556 Tourmente, M., P. Villar-Moya, E. Rial and E. R. Roldan (2015). "Differences in ATP Generation Via
557 Glycolysis and Oxidative Phosphorylation and Relationships with Sperm Motility in Mouse Species." J Biol
558 Chem **290**(33): 20613-20626.
559 Travis, A. J., C. J. Jorgez, T. Merdiushev, B. H. Jones, D. M. Dess, L. Diaz-Cueto, B. T. Storey, G. S. Kopf and
560 S. B. Moss (2001). "Functional relationships between capacitation-dependent cell signaling and
561 compartmentalized metabolic pathways in murine spermatozoa." J Biol Chem **276**(10): 7630-7636.
562 Ursini, F., S. Heim, M. Kiess, M. Maiorino, A. Roveri, J. Wissing and L. Flohé (1999). "Dual function of the
563 selenoprotein PHGPx during sperm maturation." Science **285**(5432): 1393-1396.
564 van Dijk, D., R. Sharma, J. Nainys, K. Yim, P. Kathail, A. J. Carr, C. Burdziak, K. R. Moon, C. L. Chaffer, D.
565 Pattabiraman, B. Bierie, L. Mazutis, G. Wolf, S. Krishnaswamy and D. Pe'er (2018). "Recovering Gene
566 Interactions from Single-Cell Data Using Data Diffusion." Cell **174**(3): 716-729 e727.
567 Vernet, P., R. J. Aitken and J. R. Drevet (2004). "Antioxidant strategies in the epididymis." Mol Cell
568 Endocrinol **216**(1-2): 31-39.

569 Visconti, P. E. (2012). "Sperm bioenergetics in a nutshell." Biol Reprod **87**(3): 72.
570 Zhou, R., A. S. Yazdi, P. Menu and J. Tschopp (2011). "A role for mitochondria in NLRP3 inflammasome
571 activation." Nature **469**(7329): 221-225.

572

573

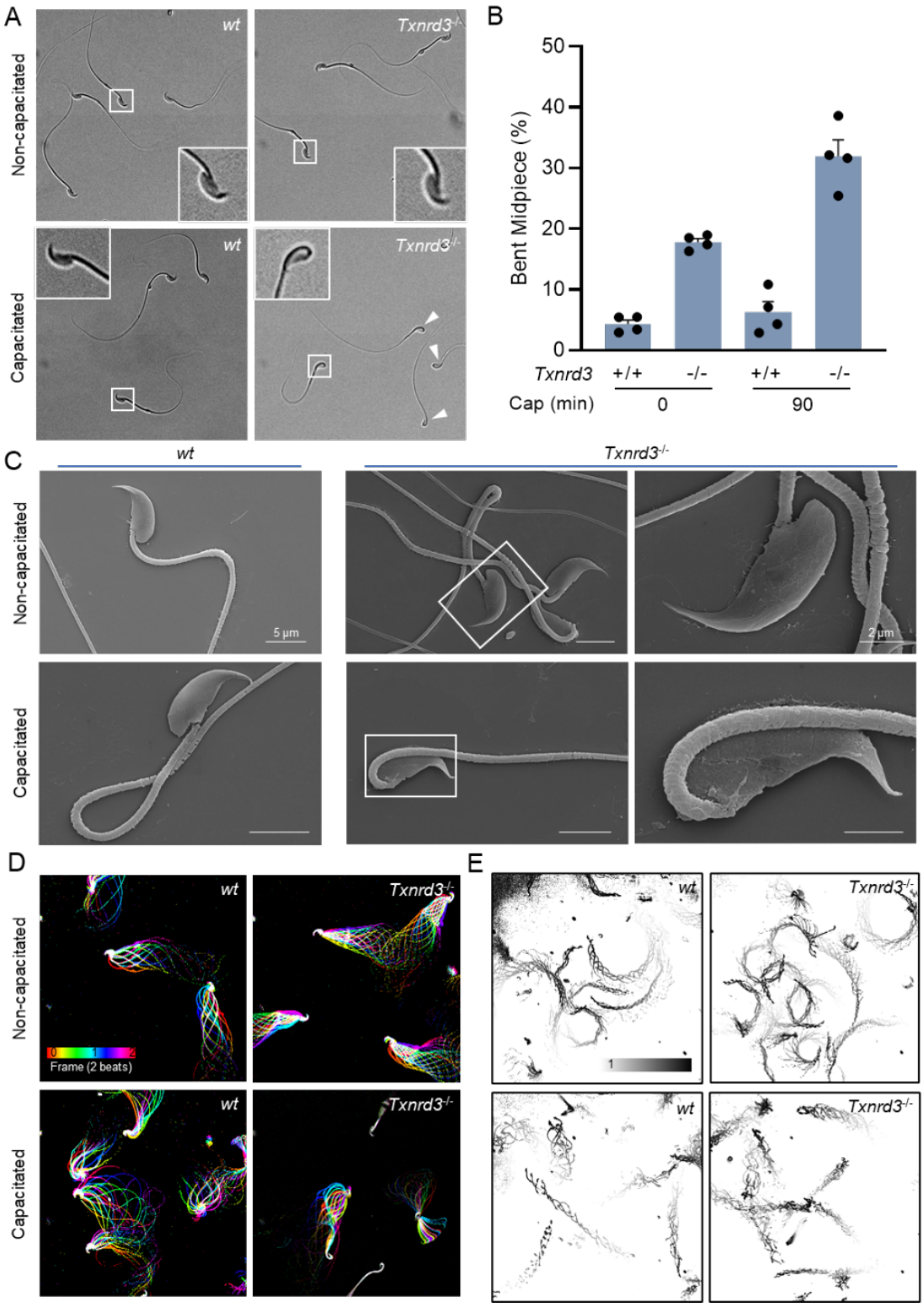

574

575 **Figure 1. TXNRD3-deficient sperm are morphologically abnormal with impaired**
576 **hyperactivated motility.** (**A**) TXNRD3-deficient sperm exhibit abnormal hairpin morphology

577 following 90 min incubation under capacitation conditions. (**B**) Quantification of abnormal hairpin
578 morphology from **A**. Mean ± SEM, n = X each group. $^{**}p < 0.01$ (**C**) Representative scanning
579 electron microscopy (SEM) images of cauda epididymal sperm. (**D**) Aligned flagellar waveform
580 traces. Movies recorded at 200 fps: *wt* and *Txnrd3*$^{-/-}$ sperm cells attached on glass coverslips before
581 (top) and after (bottom) 90 min capacitation. Overlays of flagellar traces from two beat cycles are
582 generated by hyperstacking binary images; time coded in color. (**E**) Free swimming trajectory
583 analysis. Head trace of free swimming *wt* and *Txnrd3*$^{-/-}$ sperm cells at 0 min (top) and 90 min
584 (bottom) after capacitation. Traces are from 1 s movies taken at 37°C.

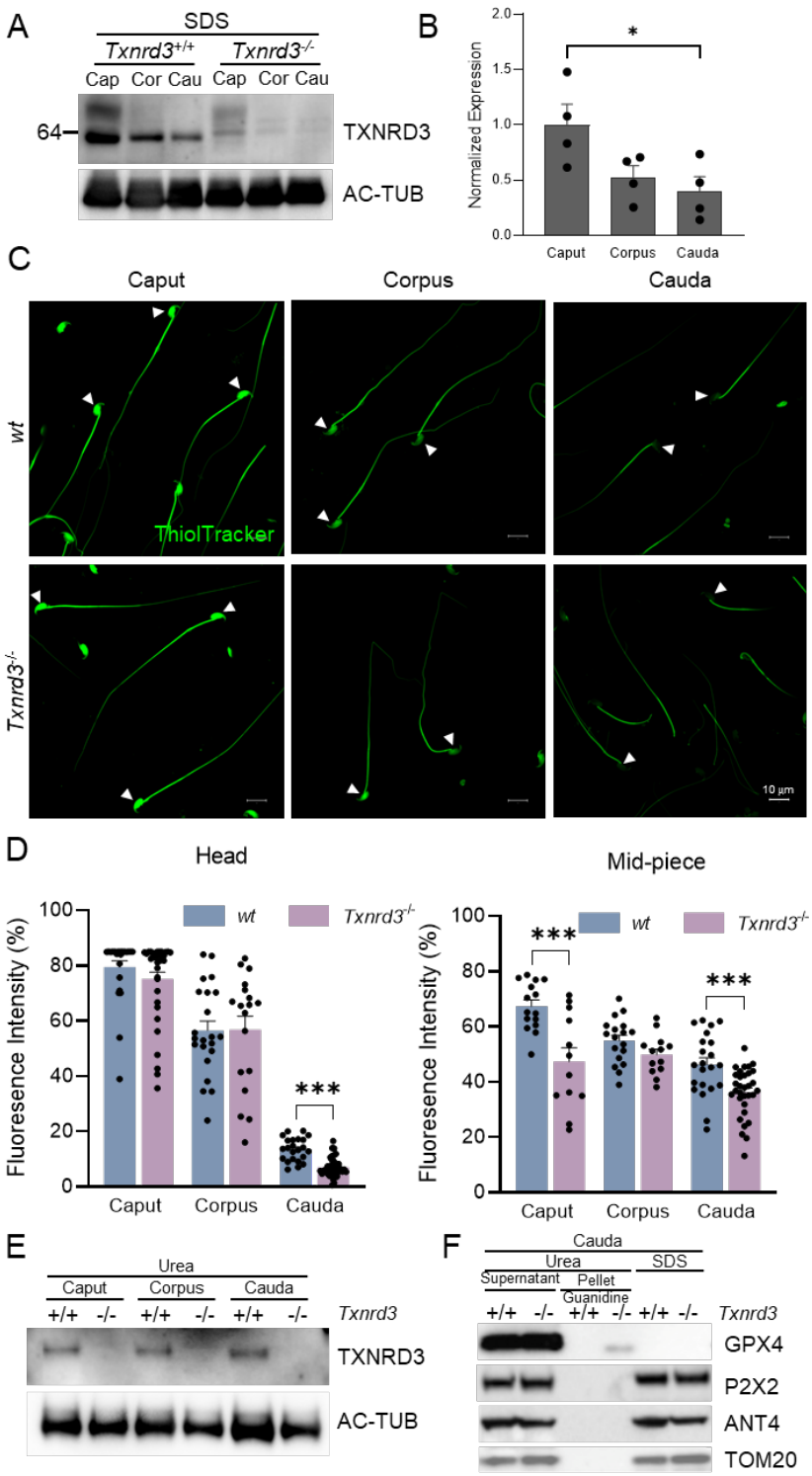

585

586 **Figure 2. Free thiol level and oxidative status are altered in *Txnrd3*$^{-/-}$ spermatozoa.** (**A**)
587 TXNRD3 expression decreased in concert with sperm maturation in the epididymis. (**B**)
588 Quantification of TXNRD3 expression from (A). (**C**) Free thiol groups level in epididymal sperm

589 from *wt* and *Txnrd3*$^{-/-}$ mice. Spermatozoa isolated from the caput, corpus and cauda epididymis
590 were incubated with ThiolTracker. (**D**) Relative quantification of free thiol levels in sperm head
591 and midpiece. (**E**) TXNRD3 are equally extracted by urea from cauda sperm. (**F**) GPx4, a potential
592 TXNRD3 substrate, exhibited stronger resistance to lysis buffer in the absence of TXNRD3. Other
593 mitochondrial or midpiece localized proteins such as ANT4, P2X2 and TOM20 were well
594 solubilized in all detergents tested.
595

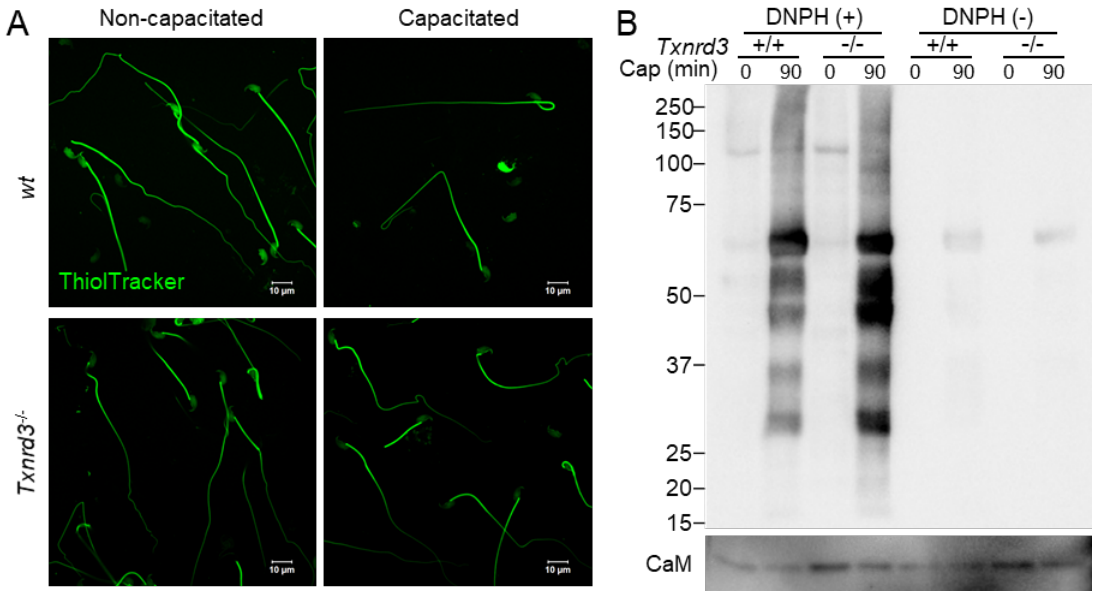

596

597 **Figure 3. TXNRD3-deficient sperm undergo more oxidation after capacitation.** (**A**) Free thiol
598 groups level revealed with ThiolTracker in cauda epididymal sperm from wide type and *Txnrd3*$^{-/-}$
599 mice before and after 90 min capacitation. (**B**) Protein carbonylation level in *wt* and *Txnrd3*$^{-/-}$
600 sperm before and after capacitation. The carbonyl groups derivatized by DNPH (2, 4 dinitrophenyl
601 hydrazine) were detected by western blotting using DNP antibody.

602

603

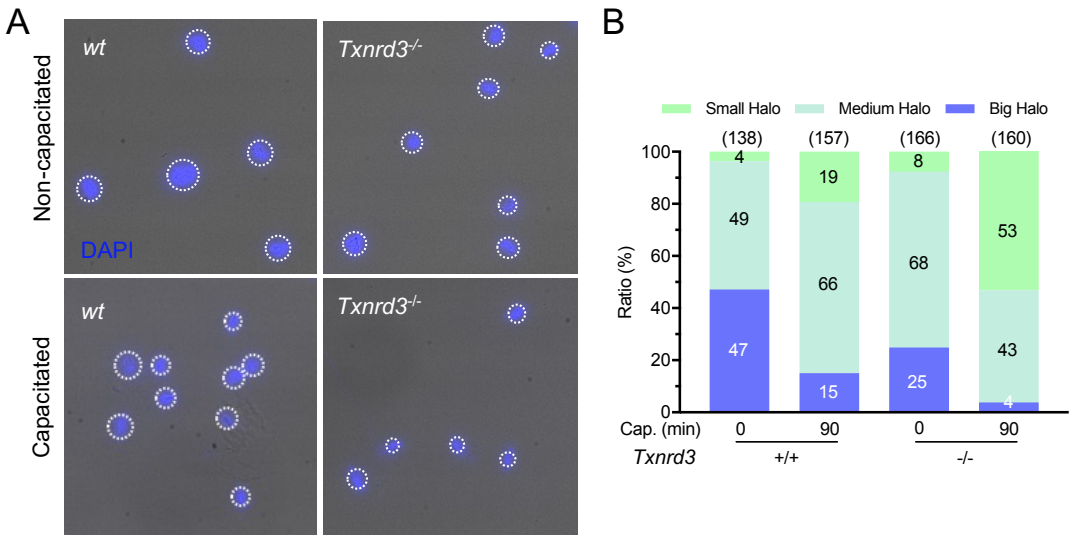

604 **Figure 4. TXNRD3-deficient sperm are more stable and resistant to acid denaturation after**
605 **capacitation.** (**A**) Sperm chromatin dispersion test show smaller halo in *Txnrd3*$^{-/-}$ sperm than in
606 *wt* sperm during capacitation, indicating extensive fragmented DNA after acid denaturation during
607 the assay procedure. DAPI (Blue). (**B**) Quantification of various halo size from *wt* and *Txnrd3*$^{-/-}$
608 sperm before and after capacitation. Based on sperm head size (~8 µm), halo sizes which are <12
609 µm (50% larger), <17 µm (100% larger) and >17 µm are divided into small, medium and big,
610 respectively.

611

612

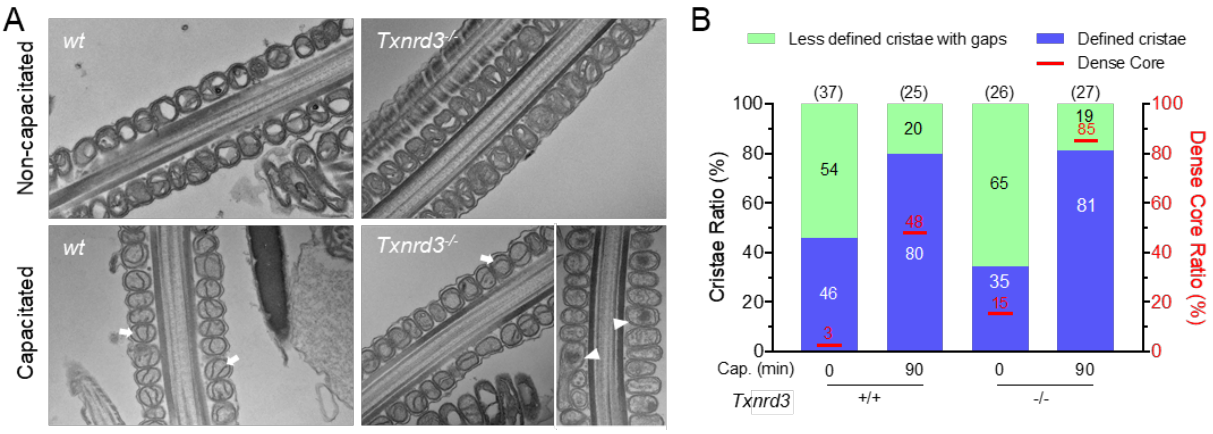

613 **Figure 5. Ultrastructural analysis of epididymal sperm.** (**A**) Representative transmission
614 electron microscopy (TEM) images of cauda epididymal sperm mitochondria. Arrows indicate
615 defined cristae found in mitochondria of capacitated sperm; arrow heads indicate dense cores
616 found in mitochondria of *Txnrd3*$^{-/-}$ sperm. (**B**) Classification of mitochondrial morphology in *wt*
617 and *Txnrd3*$^{-/-}$ sperm before and after capacitation.

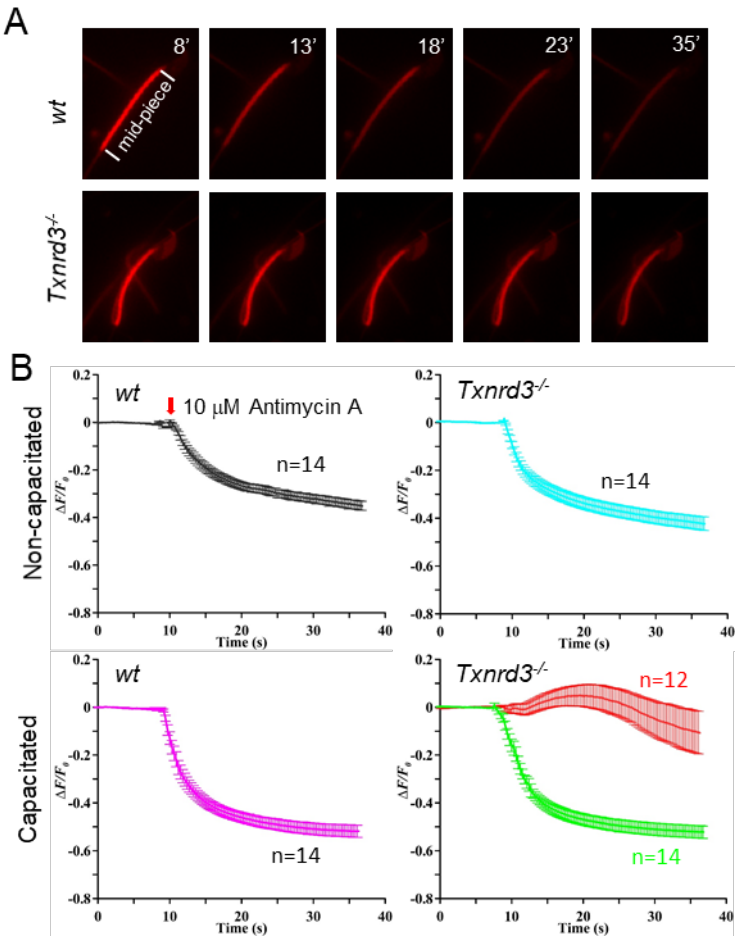

618

619 **Figure 6. Mitochondrial activity, indicated by membrane potential, is impaired in absence of**
620 **TXNRD3.** (**A**) Dynamic representative of mitochondrial membrane potential (ΔΨm) indicated by
621 Mitotracker. Mouse sperm were stained with 500 nM Mitotracker Deep Red which accumulates
622 ΔΨm-dependently. (**B**) Transition of the mitochondrial membrane potential. The changes of
623 fluorescence intensity were calculated as $\Delta F/F_0$ (F_0, the mean fluorescence intensity of the sperm
624 midpiece before adding Antimycin A (at 10 s), an inhibitor of electron transport chain; F, the
625 fluorescence of the midpiece after adding antimycin A; $\Delta F=F-F_0$). Capacitated *Txnrd3*$^{-/-}$ sperm
626 show heterogeneous response to antimycin A, suggesting disrupted cellular respiration.

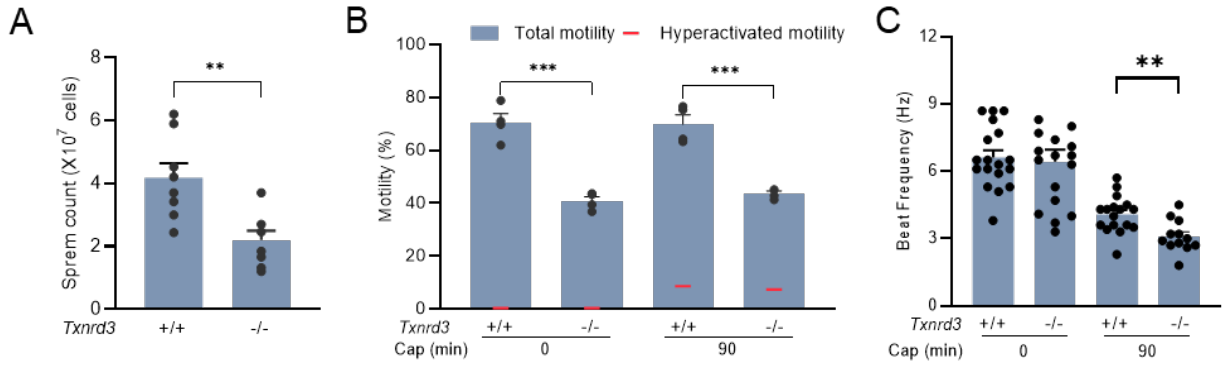

627

628 **Supplementary Figure 1. TXNRD3-deficient mice exhibit reduced sperm count and motility.**
629 (**A**) Epididymal sperm count (Mean ± SEM) from littermates at ages of 3-4 months of age. (**B**)
630 Sperm total motility and hyperactivated motility before and after incubating under capacitation
631 conditions. (**C**) Flagellar beat frequency of *wt* and *Txnrd3*$^{-/-}$ sperm before (0 min, *wt*, 6.6 ± 0.3 Hz;
632 *Txnrd3*$^{-/-}$, 6.4 ± 0.5 Hz) and after (90 min, *wt*, 4.1 ± 0.2 Hz; *Txnrd3*$^{-/-}$, 3.1 ± 0.2 Hz) capacitation.
633 Mean ± SEM, n = X each group. $^{**}p < 0.01$, $^{***}p < 0.001$.

634 **Supplementary Video 1. Head-tethered sperm from *wt* and *Txnrd3*$^{-/-}$ mice before and after**
635 **incubating under capacitation conditions.**

636 **Supplementary Video 2. Free-swimming sperm from *wt* and *Txnrd3*$^{-/-}$ mice before and after**
637 **incubating under capacitation conditions.**

638

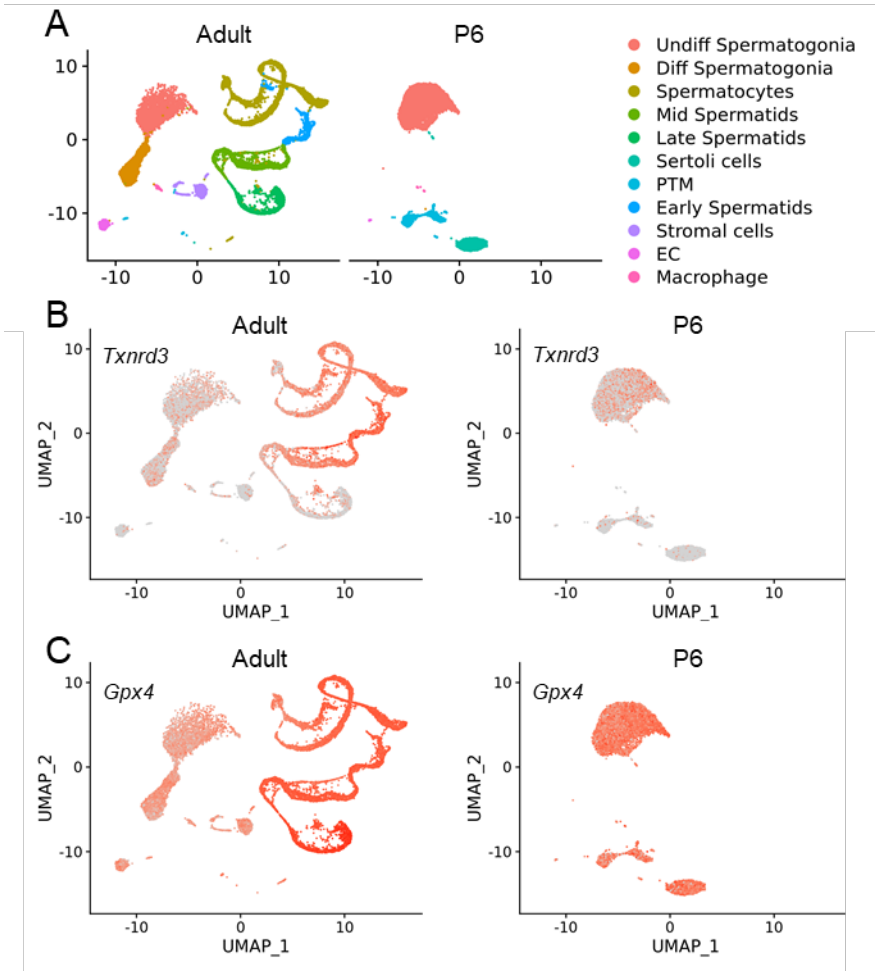

Supplementary Figure 2. Single testicular cell transcriptome profiling from adult and postnatal day 6 (P6) mice. (**A**) Clustering analysis of combined single-cell transcriptome data from testes. Each dot represents a single cell and is colored according to its cluster identity as indicated on the figure key. 11 cluster identities were assigned based on marker gene expression. PTM, Peritubular myoid; EC, Testicular endothelial cells. (**B**) Expression patterns of *Txnrd3* which is highly expressed in spermatogonia and spermatocytes but much less in spermatids. Red indicates high expression and gray indicates low or no expression. (**C**) Expression patterns of *Gpx4,* which is abundant through spermatogenesis.

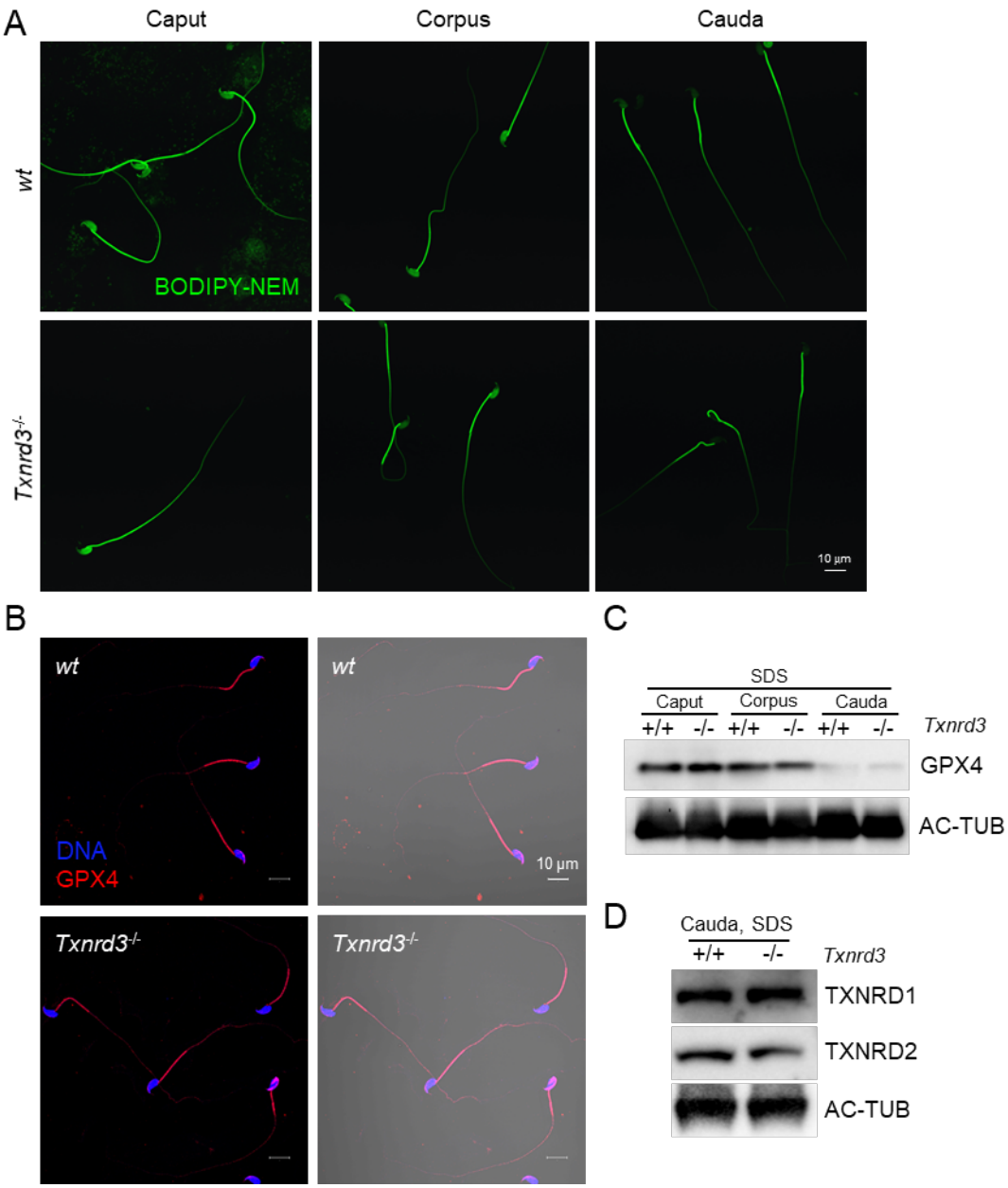

Supplementary Figure 3. Free thiol level and level of GPX4 from caput to cauda sperm. (**A**) Spermatozoa isolated from the caput, corpus and cauda epididymis were incubated with Bodipy-labeled NEM. After quenching with β-mercaptoethanol, free thiol groups in the cells were visualized using confocal microscope. (**B**) Localization of GPx4 (**C**) GPx4 shows descending level in sperm during epididymal transit. (**D**) TXNRD1 and TXNRD2 show same level in both wide type and *Txnrd3*$^{-/-}$ sperm.

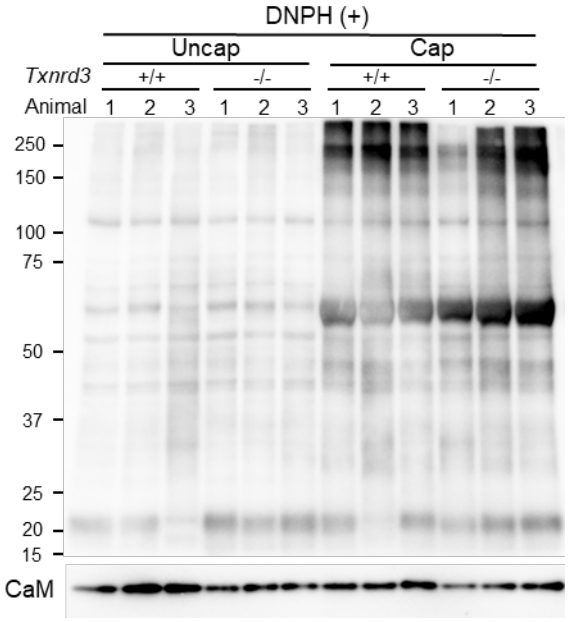

657

658 **Supplementary Figure 4. Protein oxidation status probed by protein carbonylation level is**
659 **changed during sperm capacitation.** Protein carbonylation level was detected in *wt* and Txnrd3-
660 /- sperm before and after capacitation from multiple mice.

661

662

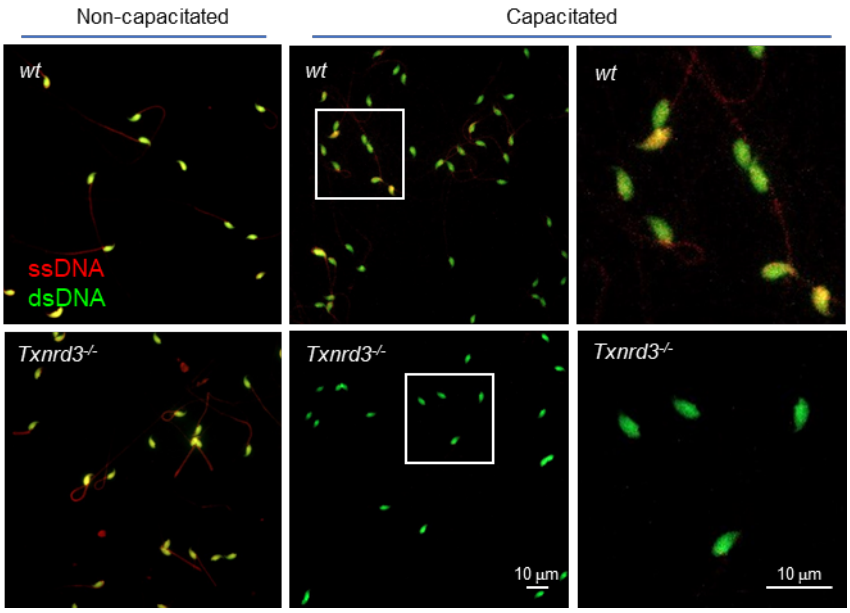

663 **Supplementary Figure 5. Evaluation of DNA state by Acridine Orange assay.** After HCl
664 incubation, *Txnrd3*$^{-/-}$ sperm generated less single-stranded DNA after capacitation, indicating more
665 resistance to acid denaturation. Single-stranded DNA (Red), double-stranded DNA (Green).
666

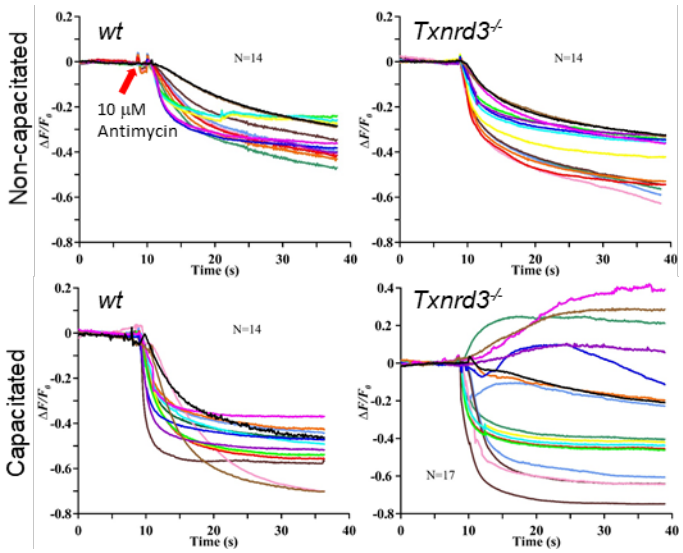

Supplementary Figure 6. Individual traces of mitochondrial membrane potential transition from wild type and *Txnrd3*$^{-/-}$ sperm. Presented are the traces of the individual sperm cells for Figure 6B.